Contents lists available at SciVerse ScienceDirect

# Journal of Power Sources

journal homepage: www.elsevier.com/locate/jpowsour

# Synthesis of Co$_2$SnO$_4$@C core–shell nanostructures with reversible lithium storage

Yue Qi, Ning Du, Hui Zhang, Ping Wu, Deren Yang *

State Key Lab of Silicon Materials and Department of Materials Science and Engineering, Zhejiang University, Hangzhou 310027, People's Republic of China

## ABSTRACT

This paper reports the synthesis of Co$_2$SnO$_4$@C core–shell nanostructures through a simple glucose hydrothermal and subsequent carbonization approach. The as-synthesized Co$_2$SnO$_4$@C core–shell nanostructures have been applied as anode materials for lithium-ion batteries, which exhibit improved cyclic performance compared to pure Co$_2$SnO$_4$ nanocrystals. The carbon matrix has good volume buffering effect and high electronic conductivity, which may be responsible for the improved cyclic performance.

© 2011 Elsevier B.V. All rights reserved.

## 1. Introduction

Rechargeable lithium-ion batteries are currently the dominant power source for portable electronic devices and considered to be the prime candidate for the next generation of electric vehicles [1]. Graphite is now used as anode materials in most commercial Li-ion batteries. However, the limited gravimetric capacity (372 mAh g$^{-1}$) of carbon has prompted intensive research for alternative anode materials that have large capacity at low potentials [2]. Since the discovery of 3$d$ transition-metal oxides with good performance as the anode materials of Li-ion batteries, a great effort has been made to improve their capacity and cycling performance [3]. Among them, cobalt oxides (Co$_3$O$_4$, CoO) demonstrated the best electrochemical properties in Li-ion batteries, compared to nickel oxide and iron oxides [4–6]. Many efforts were made to replace cobalt partially by environment-friendly and less-expensive alternative metals to lower the toxicity and reduce the cost [7–9]. As a result, the ternary cobalt-based metal compounds such as Co$_2$SnO$_4$ have been realized as anode materials of Li-ion batteries [10–12]. In this compound, the oxidation and reduction reactions are involved for cobalt oxides, and lithium alloying exists in the subsequent reaction of the tin oxides. Such multi-electron reactions in the electrochemical processes lead to higher electrochemical capacity. Recently, extensive work has been focused on the synthesis

of metal oxide–carbon hybrid nanostructures as anode materials to enhance the lithium storage performance by introducing carbon as "buffering matrixes" [13–20]. Therefore, Co$_2$SnO$_2$–C hybrid nanostructures are expected to show the improved electrochemical performance.

Herein, we report the synthesis of Co$_2$SnO$_4$@C core–shell nanostructures through a simple glucose hydrothermal and subsequent carbonization approach. The Co$_2$SnO$_4$@C core–shell nanostructures with carbon layers of different thickness have been prepared and applied as anode materials for lithium-ion batteries, which exhibit higher lithium storage capacities and better cycling performance compared to pure Co$_2$SnO$_4$ nanocrystals.

## 2. Experimental

### 2.1. Synthesis of Co$_2$SnO$_4$ nanocrystals

All the chemicals were analytical grade without further purification. Co$_2$SnO$_4$ nanocrystals were prepared by a hydrothermal route in NaOH solution [12]. Briefly, 4 mmol CoCl$_2$·6H$_2$O and 2 mmol SnCl$_4$·5H$_2$O were dissolved into 60 ml distilled water to form a transparent solution. Then 20 ml 1 M NaOH solution was dropped into the Co–Sn mixture solution under magnetic stirring. The final solution was transferred into a 100 ml Teflon-lined stainless steel autoclave, sealed, and maintained at 250 °C for 24 h. After the reaction was finished, the resulting blue solid products were centrifuged, washed with distilled water and ethanol to remove the

---

* Corresponding author. Tel.: +86 571 87951667; fax: +86 571 87952322.
  *E-mail addresses:* qiyue1024@zju.edu.cn (Y. Qi), mseyang@zju.edu.cn (D. Yang).
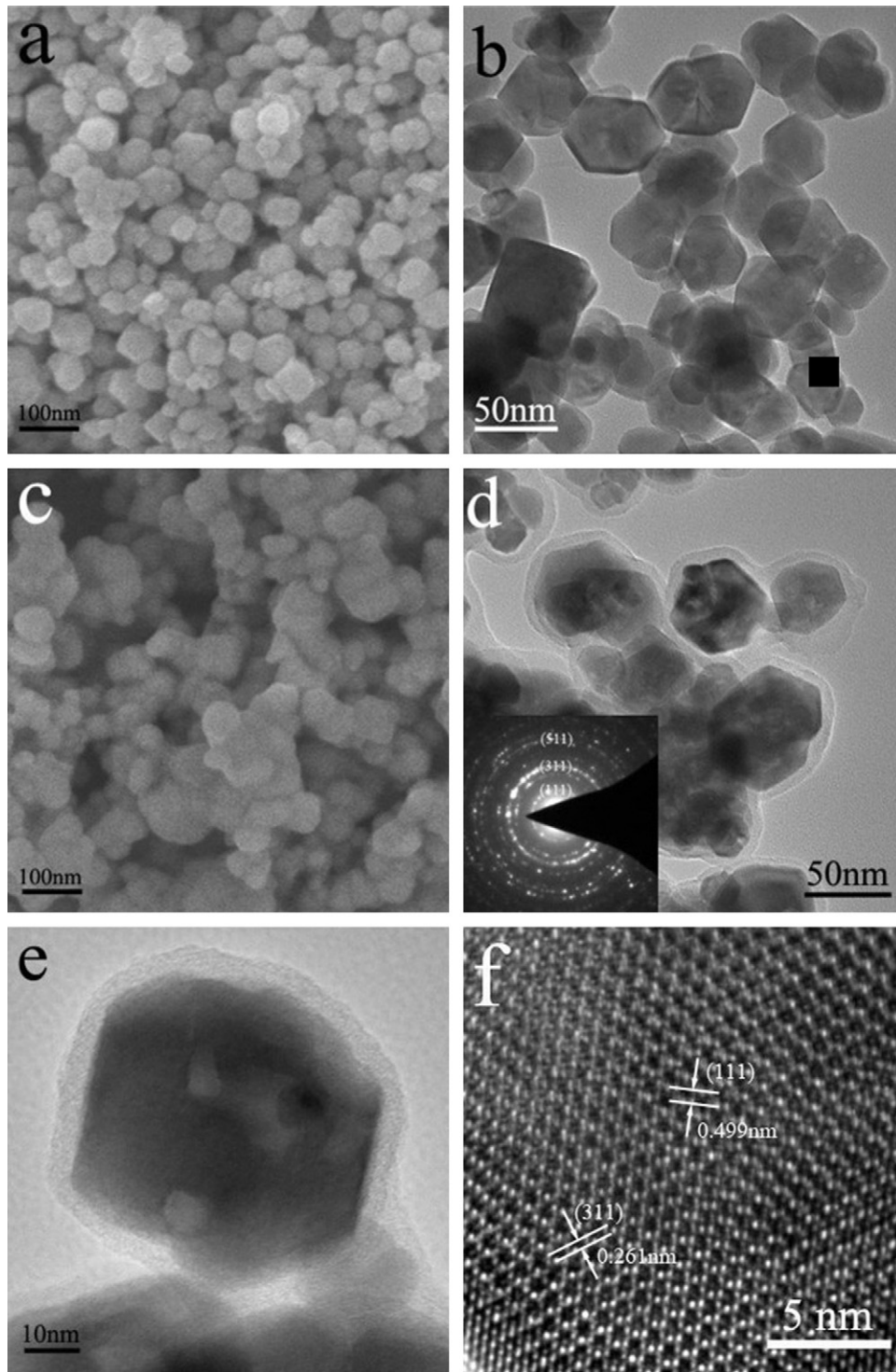
**Fig. 1.** FESEM image (a) and TEM image (b) of pure $Co_2SnO_4$ nanocrystals, and morphological and structural characterizations of $Co_2SnO_4$@C nanostructures: FESEM image (c); TEM image and its SAED pattern (inset) (d); magnified TEM image (e); HRTEM image (f).

ions possibly remaining in the final products, and finally dried at 60 °C in air.

### 2.2. Synthesis of $Co_2SnO_4$@C core–shell nanostructures

$Co_2SnO_4$@C core–shell nanostructures were prepared by a glucose hydrothermal process and subsequent carbonization approach [19,20]. Briefly, 0.4 g $Co_2SnO_4$ nanocrystals were dis-

persed in 40 ml 0.25 M aqueous glucose solution. After sonication for 20 min, the solution was transferred into a 50 ml Teflon-lined stainless steel autoclave, sealed, and maintained at 180 °C for 12 h. After the reaction was finished, the resulting solid products were centrifuged, washed with distilled water and ethanol to remove the ions possibly remaining in the final products, and then dried at 80 °C under vacuum. Finally, the products were kept in a tube furnace at 500 °C for 3 h under $N_2$ at a ramping rate of 5 °C min$^{-1}$.
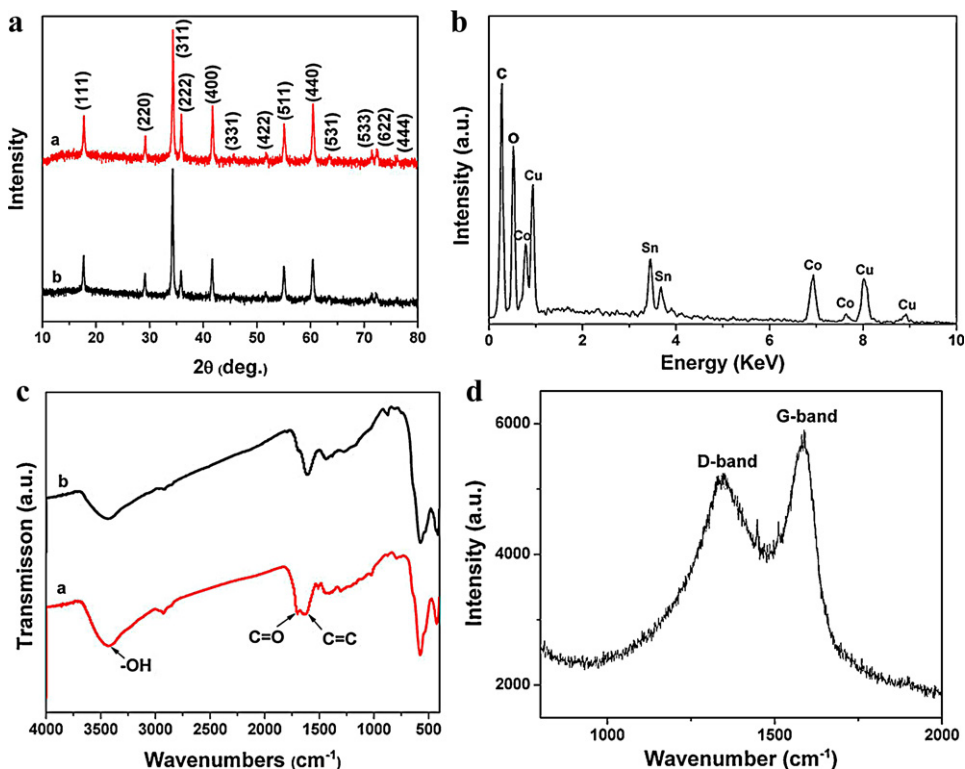
**Fig. 2.** (a) XRD patterns of pure $Co_2SnO_4$ nanocrystals (diffraction pattern *a*) and $Co_2SnO_4$@C nanostructures (diffraction pattern *b*); (b) EDX spectrum of $Co_2SnO_4$@C nanostructures; (c) infrared spectra of $Co_2SnO_4$@C nanostructures before carbonization (curve *a*) and after carbonization (curve *b*); (d) typical Raman spectrum of the $Co_2SnO_4$@C nanostructures.

## 2.3. Characterization

The obtained samples were characterized by X-ray powder diffraction (XRD) using a Rigaku D/max-ga X-ray diffractometer with graphite monochromatized Cu Kα radiation ($\gamma = 1.54178\,\text{Å}$). The morphology and structure of the samples were examined by transmission electron microscopy (TEM, JEM-200 CX, 160 kV), high-resolution transmission electron microscopy (HRTEM, JEOL JEM-2010) and field emission scanning electron microscopy (FESEM, Hitachi S-4800) with energy-dispersive X-ray spectrometer (EDX). Thermogravimetric analysis (TGA) was tested on SDT Q600 V8.2 Bulid 100. The infrared (IR) spectra were measured with a Nicolet Nexus FTIR 670 spectrophotometer. The Raman spectroscopy measurement was carried out on a Labor Raman HR-800 Raman spectrometer system.

## 2.4. Electrochemical measurements of $Co_2SnO_4$@C core–shell nanostructures

Electrochemical measurements were carried out using two-electrode cells with lithium metal as the counter and reference electrodes. The working electrode was composed of the active material ($Co_2SnO_4$@C core–shell nanostructures), conductive materials (acetylene black, AB), and binder (polyvinyldifluoride, PVDF) in a weight ratio of $Co_2SnO_4$@C core–shell nanostructures/AB/PVDF = 70:15:15, and pasted on Cu foil. The electrolyte solution was 1 M $LiPF_6$ dissolved in a mixture of ethylene carbonate (EC), propylene carbonate (PC), and diethyl carbonate (DEC) with the volume ratio of EC/PC/DEC = 3:1:1. The cell assembly was performed in a glovebox filled with pure argon (99.999%) in the presence of an oxygen scavenger and a sodium drying agent. The electrode capacity was measured by a galvanostatic discharge–charge method at a current density of $100\,\text{mA}\,\text{g}^{-1}$ in the potential range of 0.01–2.5 V at 20 °C. Cyclic voltammetry (CV) were

recorded on a MSTAT4 (Arbin Instruments) system in the potential range of 0.01–2.5 V at a scan rate of $0.1\,\text{mV}\,\text{s}^{-1}$. The electrochemical impedance spectroscopy (EIS) of the electrodes was performed on a CHI660D electrochemical workstation with an ac signal of 5 mV in amplitude and the frequency ranged from 0.01 Hz to 100 kHz. Before the EIS measurement, the electrodes were cycled for five cycles, then discharged to 2.0 V and kept until the open-circuit voltage stabilized.

## 3. Results and discussion

$Co_2SnO_4$@C core–shell nanostructures were synthesized through a simple glucose hydrothermal and subsequent carbonization approach. Fig. 1 shows the morphological and structural characterizations of $Co_2SnO_4$ nanocrystals and $Co_2SnO_4$@C core–shell nanostructures. As can be seen, the polyhedral products of $Co_2SnO_4$ nanocrystals were uniform with a particle size less than 100 nm (Fig. 1a and b). Compared with the naked $Co_2SnO_4$ nanocrystals, the $Co_2SnO_4$@C core–shell nanostructures retained the polyhedral shape after coating of a carbon-rich layer (Fig. 1c and d). The TEM images (Fig. 1d and e) indicate that the uniform coating layer is smooth and continuous and the thickness of the layer is about 5–10 nm. The $Co_2SnO_4$@C core–shell nanostructures can be confirmed by its selected-area electron diffraction (SAED) pattern (Fig. 1d, inset). As observed, there are three diffraction rings corresponding to the (1 1 1), (3 1 1), and (5 1 1) planes of $Co_2SnO_4$, respectively. HRTEM was employed to further characterize the $Co_2SnO_4$@C core–shell nanostructures. As can be seen from Fig. 1f, there are two kinds of lattice fringes with lattice spacings of about 0.499 and 0.261 nm, corresponding to (1 1 1) and (3 1 1) planes of $Co_2SnO_4$ nanoparticles, respectively.

Fig. 2a shows the XRD patterns of pure $Co_2SnO_4$ nanocrystals (diffraction pattern *a*) and $Co_2SnO_4$@C core–shell nanostructures

(diffraction pattern *b*). It can be seen from the diffraction pattern *a* that all the diffraction peaks can be indexed to cubic spinel structured $Co_2SnO_4$, consistent with the values in the standard card (JCPDS: 48-1719). After surface coating, the diffraction peaks remain unchanged due to the amorphous nature of the carbon layer. Fig. 2b shows the EDX spectrum taken from the $Co_2SnO_4$@C core–shell nanostructures. As observed, the strong peaks for C, O, Co, and Sn elements are expected from the carbon layer and $Co_2SnO_4$ nanocrystals, respectively, while the Cu peaks come from the sample stage used in the FESEM measurements. IR spectroscopy was employed to further investigate the carbonization process. After a glucose hydrothermal process, $Co_2SnO_4$ nanoparticles were coated with glucose-derived carbon-rich polysaccharide (GCP) layer. Subsequently, the GCP layer was fully carbonized to a carbon layer under an inert atmosphere, resulting in $Co_2SnO_4$@C core–shell nanostructures. It can be seen from Fig. 2c (curve *a*) that the stretching vibrations at 1700 and 1625 $cm^{-1}$ can be attributed to C=O and C=C vibrations, respectively, indicating aromatization of glucose during the hydrothermal treatment [21,22]. After thermal carbonization processes, the GCP layer from $Co_2SnO_4$@C core–shell nanostructures has been fully carbonized to a carbon layer, leading to the disappearance of C=O vibrations peaks, which can be confirmed from the curve *b*. Raman spectroscopy measurement was used to further confirm the graphitization state of carbon layer. Fig. 4d shows the Raman spectrum of $Co_2SnO_4$@C-thick. A broad peak at 1340 $cm^{-1}$ as well as a sharp peak at 1580 $cm^{-1}$ can be clearly observed. The peak at 1340 $cm^{-1}$ is usually attributed to the vibrations of carbon atoms with dangling bonds for the in-plane terminations of disordered graphite and is marked as the D-band, and the peak at 1580 $cm^{-1}$ (marked as G-band) (corresponding to the $E_{2g}$ mode) is closely associated to the vibration in all $sp^2$ bonded carbon atoms in a 2-dimensional hexagonal lattice, such as in a graphite layer [23]. The intensity ratio of the D to G band ($I_D/I_G$) is calculated to be 0.88, reflecting the relative disorder and low graphitic crystallinity of the carbon layer. This result coincides with that of XRD, SAED, and TEM analyses.

The thickness of carbon layer can be adjusted by the hydrothermal time. Fig. 3a and b shows the TEM images of $Co_2SnO_4$@C core–shell nanostructures prepared for different time. It can be seen that the thickness of the carbon layer is about 2–3 nm after a 4 h hydrothermal reaction (Fig. 3a). When the reaction time was prolonged to 12 h, the thickness of carbon layer increased to 5–10 nm (Fig. 3b). TGA was performed to determine the amount of carbon present in the samples. As can be observed from Fig. 3c, the weight loss at 250–600 °C could be attributed mainly to the removal of the carbon layer. Thus, the carbon contents of $Co_2SnO_4$@C core–shell nanostructures prepared for 4 h and 12 h are determined to be about 10.5% and 25.2% by weight, respectively, which is consistent with TEM analysis.

The as-synthesized $Co_2SnO_4$@C core–shell nanostructures were used as potential anode materials for lithium-ion batteries. Fig. 4a shows the first three cyclic voltammogram (CV) curves of $Co_2SnO_4$@C core–shell nanostructure electrodes in the potential range of 0.01–2.5 V at a slow scan rate of 0.1 mV s$^{-1}$. The CV curves are in good agreement with the previous reported $Co_2SnO_4$ anodes [10–12]. It is generally accepted that the electrochemical process of $Co_2SnO_4$ anodes can be described by the following principal reactions:

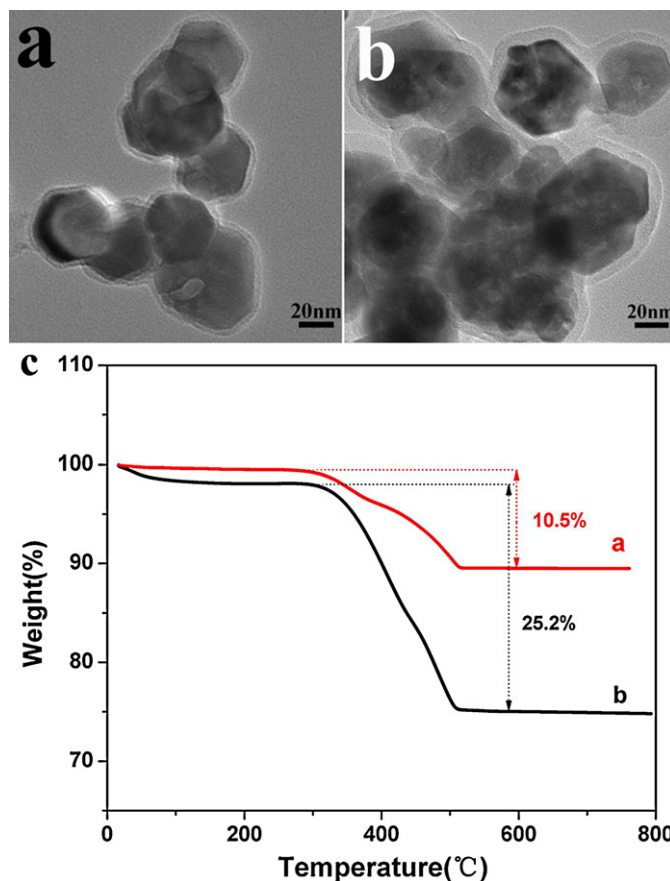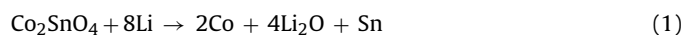$$Co_2SnO_4 + 8Li \rightarrow 2Co + 4Li_2O + Sn \tag{1}$$

$$Sn + 4.4Li \leftrightarrow Li_{4.4}Sn \tag{2}$$

$$Sn + 2Li_2O \leftrightarrow SnO_2 + 4Li \tag{3}$$

$$Co + Li_2O \leftrightarrow CoO + 2Li \tag{4}$$



**Fig. 3.** TEM images of (a) $Co_2SnO_4$@C-thin and (b) $Co_2SnO_4$@C-thick nanostructures; (c) TGA analysis of the $Co_2SnO_4$@C-thin (curve *a*) and $Co_2SnO_4$@C-thick nanostructures (curve *b*).

In the first cycle, there is a clear reduction peak at the potential of 0.6 V which can be attributed to the decomposition of $Co_2SnO_4$, and the formation of $Li_2O$ and the SEI film [24,25]. The peak in the cathodic process at 0.07 V is attributed to the formation of $Li_{4.4}Sn$ [19]. In the first anodic process, three oxidation peaks at 0.57, 1.3, and 2.1 V are attributed to the de-alloying process (0.57 V), the re-oxidation of tin (1.3 V) and cobalt (2.1 V) [6,19], respectively. In the second and third cycles, there are three characteristic pairs (cathodic, anodic) of current peaks at the potential of (0.07/0.57 V), (0.7/1.3 V) and (1.3/2.1 V), corresponding to the alloying/de-alloying process of $Li_{4.4}Sn$, and the redox reactions of $Sn/SnO_2$ and $Co/CoO$, respectively.

Fig. 4b displays the 1st, 35th, and 75th discharge–charge curves of the $Co_2SnO_4$@C-thick core–shell nanostructure based anode material at a current density of 100 mA g$^{-1}$ at room temperature. The discharge curve of the first cycle has an extended potential plateaus at about 0.8 V, followed by two sloping potentials at about 0.5 V and 0.3 V. The discharge capacities of the electrode in the 1st, 35th, and 75th cycles were 1378, 541, and 474 mAh g$^{-1}$. The uniform and continuous carbon buffering matrix, which can effectively alleviate volume expansion/contraction during cycling, may be responsible for the enhanced cycling performance of $Co_2SnO_4$@C-thick core–shell nanostructures. Fig. 5a shows the discharge capacity versus cycle number for the $Co_2SnO_4$ nanocrystals, the $Co_2SnO_4$@C-thick and $Co_2SnO_4$@C-thin core–shell nanostructures based anode materials at a current density of 100 mA g$^{-1}$ at room temperature. The capacity of $Co_2SnO_4$@C-thick core–shell nanostructures maintained at 474 mAh g$^{-1}$ after 75 discharge/charge cycles with a capacity retention of 60.4% compared with the first reversible capacity, which was much higher than that of
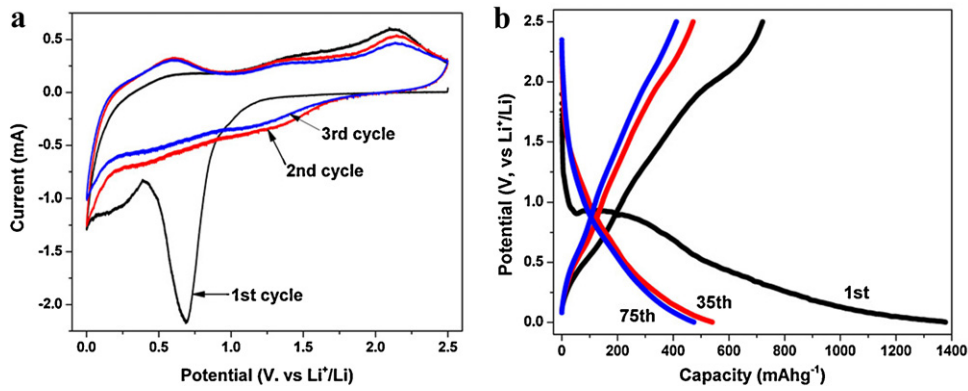
**Fig. 4.** (a) The first three CV curves of $Co_2SnO_4$@C nanostructures in the potential range of 0.0–2.5 V at a scan rate of 0.1 mV s$^{-1}$; (b) The 1st, 35th, and 75th discharge–charge curves of the $Co_2SnO_4$@C-thick nanostructures based anode material at a current density of 100 mA g$^{-1}$ at room temperature.
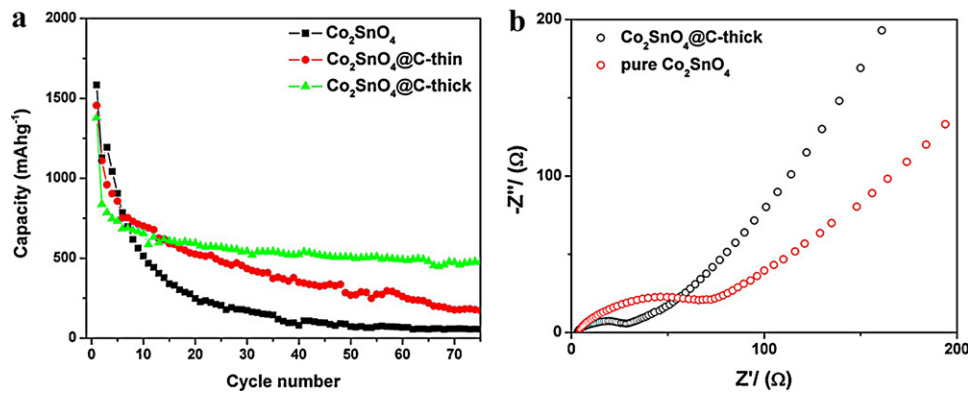


**Fig. 5.** (a) Discharge capacity versus cycle number for the $Co_2SnO_4$ nanocrystals, the $Co_2SnO_4$@C-thick and $Co_2SnO_4$@C-thin nanostructures based anode materials at a current density of 100 mA g$^{-1}$ at room temperature. (b) Nyquist plots of $Co_2SnO_4$ and $Co_2SnO_4$@C electrodes obtained by applying a sine wave with amplitude of 5 mV over the frequency range 100 kHz to 0.01 Hz.

$Co_2SnO_4$@C-thin core–shell nanostructures (173 mAh g$^{-1}$ with the capacity retention of 15.6%) and $Co_2SnO_4$ nanocrystals (56 mAh g$^{-1}$ with the capacity retention of 5.0%), suggesting that the volume buffering effect of the thin carbon layer was not apparent. Therefore, the thickness and uniformity of the carbon layer should be carefully determined for optimized lithium storage performance [15,20,26].

EIS was used to understand the relevance of morphology and surface area of the $Co_2SnO_4$ and $Co_2SnO_4$@C-thick electrodes with the electrochemical performance in terms of the total internal electrochemical impedances of a cell. The characteristic impedance curves (Nyquist plots) for the two electrodes are shown in Fig. 5b. In impedance spectroscopy, the high frequency semicircle is attributed to the SEI film and/or contact resistance, the semicircle
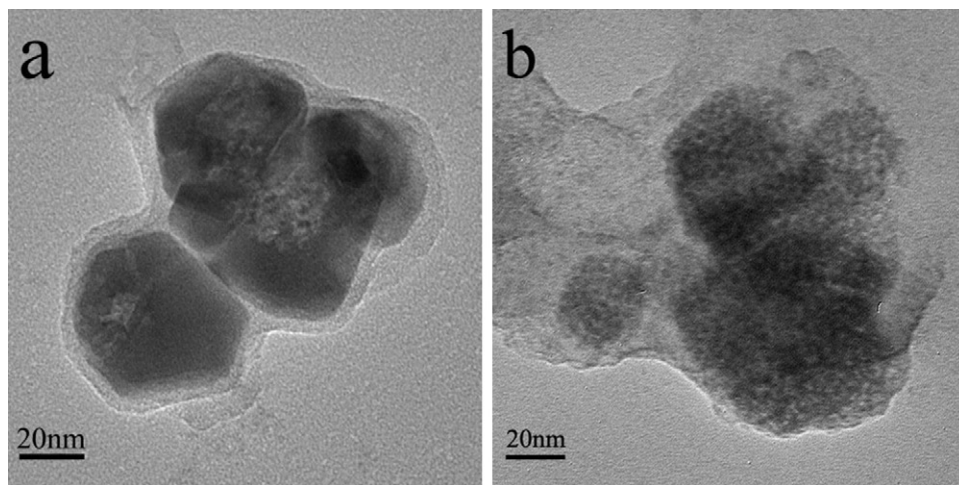


**Fig. 6.** TEM images of the $Co_2SnO_4$@C-thick and $Co_2SnO_4$@C-thin nanostructures after 20 discharge/charge cycles: (a) $Co_2SnO_4$@C-thick nanostructures and (b) $Co_2SnO_4$@C-thin nanostructures.

in medium frequency region is assigned to the charge-transfer impedance on electrode/electrolyte interface, and the inclined line at an approximate 45° angle to the real axis corresponds to the lithium-diffusion process within electrodes [27,28]. It is shown that the diameter of the semicircle in medium frequency region for the $Co_2SnO_4$@C-thick electrode is smaller than that of $Co_2SnO_4$ electrode, revealing lower charge-transfer impedances. This indicates that the charge-transfer process of the $Co_2SnO_4$@C-thick electrode was improved after the incorporation of carbon. The thickness of SEI film over active electrode affects the performance of a given electrode, since a very thick layer may prevent the effective charge transfer and diffusion process [29]. The $Co_2SnO_4$@C-thick sample showed smaller high frequency semicircle, which indicated lower surface resistance and may be attributed to a thinner surface film. Due to the larger slope of inclined line in impedance spectroscopy, the lithium-diffusion process of the $Co_2SnO_4$ electrode has also been improved after combination with the carbon layer electrode which leads to fast charge/discharge capability and enhanced electrochemistry performance. The carbon can also keep the $Co_2SnO_4$ active material stable during the charge–discharge cycling.

The structural stability of nanoelectrode materials during cycling played a critical role in their cycling performance, which can be confirmed by morphologies of the electrode materials after cycling. Fig. 6 shows the TEM images of $Co_2SnO_4$@C-thick and $Co_2SnO_4$@C-thin core–shell nanostructures anode materials after 20 discharge/charge cycles. As observed, the $Co_2SnO_4$@C-thick core–shell nanostructures remained unbroken, whereas the morphology of the $Co_2SnO_4$@C-thin core–shell nanostructures was destroyed, which can explain the huge differences in the lithium storage property of $Co_2SnO_4$@C-thick and $Co_2SnO_4$@C-thin core–shell nanostructures.

## 4. Conclusions

In summary, we have synthesized $Co_2SnO_4$@C core–shell nanostructures through a simple glucose hydrothermal and subsequent carbonization approach. The $Co_2SnO_4$@C core–shell nanostructures markedly improved cyclic performance compared to pure $Co_2SnO_4$ nanocrystals, which can be attributed to the uniform and continuous carbon buffering matrix. Moreover, $Co_2SnO_4$@C-thick shows the better cyclic performance than $Co_2SnO_4$@C-thin because of the more stable structure during the charge–discharge process.

## References

[1] J. Goodenough, Y. Kim, Chem. Mater. 22 (2010) 587–603.
[2] J.M. Tarascon, M. Armand, Nature 414 (2001) 359–367.
[3] P. Poizot, S. Laruelle, S. Grugeon, L. Dupont, J.M. Tarascon, Nature 407 (2000) 496–499.
[4] W.Y. Li, L.N. Xu, J. Chen, Adv. Funct. Mater. 15 (2005) 851–857.
[5] K.T. Nam, D.W. Kim, P.J. Yoo, C.Y. Chiang, N.L. Meethong, P.T. Hammond, Y.M. Chiang, A.M. Belcher, Science 312 (2006) 885–888.
[6] N. Du, H. Zhang, B.D. Chen, J.B. Wu, X.Y. Ma, Z.H. Liu, Y.Q. Zhang, D.R. Yang, X.H. Huang, J.P. Tu, Adv. Mater. 19 (2007) 4505–4509.
[7] Y.M. Kang, K.T. Kim, J.H. Kim, H.S. Kim, P.S. Lee, J.Y. Lee, H.K. Liu, S.X. Dou, J. Power Sources 133 (2004) 252–259.
[8] Y.Q. Chu, Z.W. Fu, Q.Z. Qin, Electrochim. Acta 49 (2004) 4915–4921.
[9] N. Du, Y.F. Xu, H. Zhang, J.X. Yu, C.X. Zhai, D.R. Yang, Inorg. Chem. 50 (2011) 3320–3324.
[10] P.A. Connor, J.T.S. Irvine, J. Power Sources 97 (2001) 223–225.
[11] P.A. Connor, J.T.S. Irvine, Electrochim. Acta 47 (2002) 2885–2892.
[12] G. Wang, X.P. Gao, P.W. Shen, J. Power Sources 192 (2009) 719–723.
[13] X.W. Lou, C.M. Li, L.A. Archer, Adv. Mater. 21 (2009) 2536–2539.
[14] S. Chou, J. Wang, C. Zhong, M.M. Rahman, H. Liu, S. Dou, Electrochim. Acta 54 (2009) 7519–7524.
[15] P. Wu, N. Du, H. Zhang, J.X. Yu, D.R. Yang, J. Phys. Chem. C 114 (2010) 22535–22538.
[16] M.F. Hassan, Z.P. Guo, Z. Chen, H.K. Liu, J. Power Sources 195 (2010) 2372–2376.
[17] B. Liu, Z.P. Guo, G.D. Du, Y. Nuli, M.F. Hassan, D.Z. Jia, J. Power Sources 195 (2010) 5382.
[18] J. Liu, W. Li, A. Manthiram, Chem. Commun. 46 (2010) 1437–1439.
[19] P. Wu, N. Du, H. Zhang, J.X. Yu, Y. Qi, D.R. Yang, Nanoscale 3 (2011) 746–750.
[20] P. Wu, N. Du, H. Zhang, J.X. Yu, D.R. Yang, J. Phys. Chem. C 115 (2011) 3612–3620.
[21] X. Sun, Y. Li, Angew. Chem. Int. Ed. 43 (2004) 597–601.
[22] S. Ikeda, K. Tachi, Y.H. Ng, Y. Ikoma, T. Sakata, H. Mori, T. Harada, M. Masumura, Chem. Mater. 19 (2007) 4335–4340.
[23] L. Xu, W. Zhang, Y. Ding, Y. Peng, S. Zhang, W. Yu, Y. Qian, J. Phys. Chem. B 108 (2004) 10859–10862.
[24] Y. Sharma, N. Sharma, G.V.S. Rao, B.V.R. Chowdari, J. Power Sources 173 (2007) 495–501.
[25] M. Marcinek, L.J. Hardwick, T.J. Richardson, X. Song, R. Kostecki, J. Power Sources 173 (2007) 965–971.
[26] J.S. Chen, Y.L. Cheah, Y.T. Chen, N. Jayaprakash, S. Madhavi, Y.H. Yang, X.W. Lou, J. Phys. Chem. C 113 (2009) 20504–20508.
[27] S.B. Yang, H.H. Song, X.H. Chen, Electrochem. Commun. 8 (2006) 137–142.
[28] X.H. Huang, J.P. Tu, C.Q. Zhang, J.Y. Xiang, Electrochem. Commun. 9 (2007) 1180–1184.
[29] J.X. Zhu, Y.K. Sharma, Z.Y. Zeng, X.J. Zhang, M. Srinivasan, S. Mhaisalkar, H. Zhang, H.H. Hng, Q.Y. Yan, J. Phys. Chem. C 115 (2011) 8400–8406.